J. Fluid Mech. (1990), *vol.* 216, *pp.* 437–458
Printed in Great Britain

Stability of symmetric film-splitting between counter-rotating cylinders

By D. J. COYLE†, C. W. MACOSKO AND L. E. SCRIVEN
Department of Chemical Engineering and Materials Science, University of Minnesota, Minneapolis, MN 55455, USA

(Received 12 May 1989)

The ribbing instability, an extremely common cause of non-uniform liquid films in coating operations, is investigated both theoretically and experimentally. The Navier–Stokes system for the two-dimensional flow in symmetric film-splitting in forward roll coating is solved by finite-element analysis. Stability of the flow with respect to three-dimensional disturbances is examined by applying linear stability theory in a consistent finite-element approach, taking Fourier components in the transverse direction. The resulting generalized asymmetric eigenproblem is solved for the growth rates of disturbances as functions of wavenumber. The theory accurately predicts the critical capillary number and wavenumber at the transition to large-amplitude ribs. A sensitive experimental technique for detecting the ribs was developed that relies on low-angle reflection of a focused strip of white light off the meniscus between the rolls. This allowed detection of much smaller amplitude ribs, and much smaller critical capillary numbers were measured. The results indicate that the transition to ribbing is an imperfect bifurcation due to end effects, and clarify earlier discordances in the literature.

1. Introduction

When a thin liquid layer is coated onto a solid substrate or flexible web by a process of brushing, spreading, or rolling, the end result often is not a uniform film, but instead one with a corduroy or ribbed pattern as shown in figure 1. If the viscosity is too high or the speed is too fast, the film profile transverse to the direction of coating is wavy; the crests and troughs run in the coating direction. This behaviour is a result of a flow instability that is commonly called ribbing.

This paper examines the ribbing instability in the case of symmetric film-splitting in forward roll coating when the rolls are half-submerged. In this process two rolls of equal radii (R) are held at a fixed minimum surface separation ($2H_0$) and are rotated such that the surface speeds in the gap region are equal and in the same direction. (Rolls turning at different rates or of different radii also find applications but are not treated here.) Upstream of the gap is 'flooded', i.e. there is an infinite supply of liquid and no free surface, whereas downstream the liquid layer carried through the gap splits to form two films, each coating one of the roll surfaces. It is under the free surface where the film splits that the flow is susceptible to ribbing, which is characterized by sinusoidal variations in the transverse direction (parallel to the roll axes). The appearance of ribbing indicates that the two-dimensional, steady-state

† Current address: General Electric Company, Corporate Research and Development, Schenectady, NY 12301, USA.

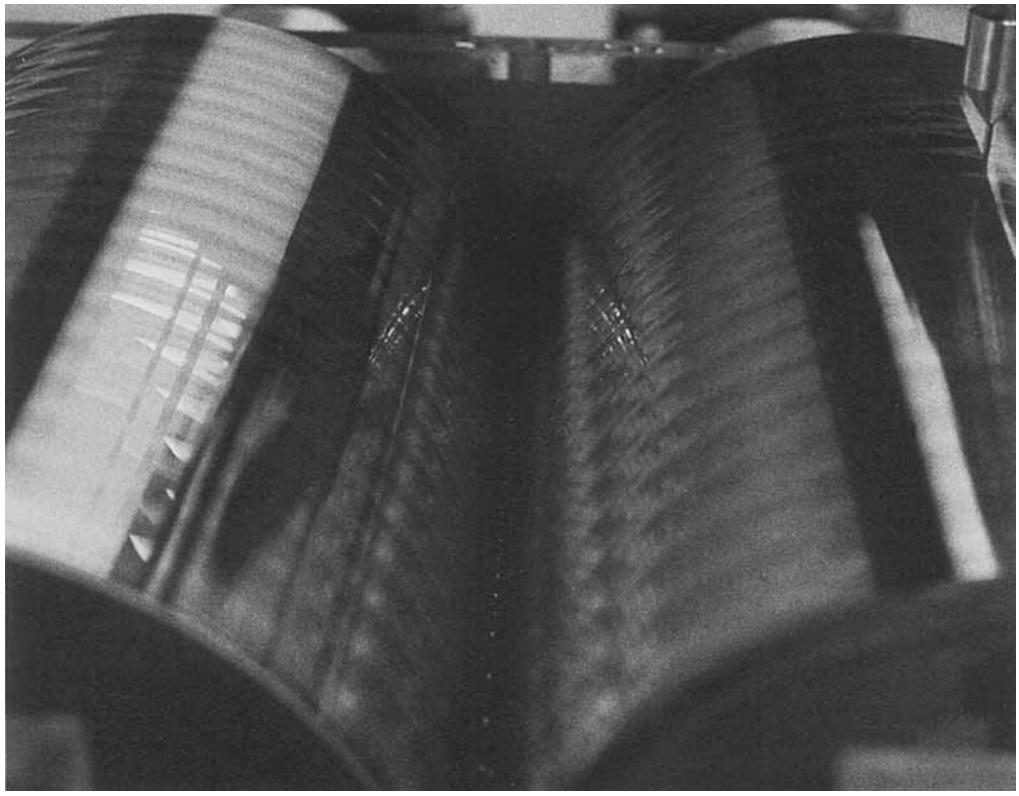

FIGURE 1. Photograph of the ribbing instability in symmetric film-splitting between half-submerged counter-rotating cylinders.

flows calculated previously (Coyle, Macosko & Scriven 1986) are not always unique or stable. At issue, then, are the regions in the space of relevant parameters where the two-dimensional flows are stable, and, more immediately, the boundary between these uniform-film flows and the ribbed flows. This boundary is the locus of points where three-dimensional ribbed flows bifurcate from the two-dimensional uniform-film flows. Our approach is both theoretical and experimental. The theory is a finite-element linear stability analysis of three-dimensional disturbances to the two-dimensional base flow. The experiments include careful visual observations of free-surface topography, both in the way used by previous researchers and by a more sensitive visualization technique.

There has been considerable interest in the phenomenon of ribbing from both scientific and technological points of view. This work has recently been reviewed by Ruschak (1985). The analysis of ribbing necessarily starts from a mathematical description of the unperturbed base state, a steady, two-dimensional viscous free-surface flow. Taylor (1963) pointed out how the steady-state flow naturally decomposes into two regions: a two-dimensional flow near the meniscus and a one-dimensional nearly rectilinear flow (sometimes referred to as 'lubrication flow') upstream. Ruschak (1982) formalized this approach by means of the method of matched asymptotic expansions, after which he solved for the two-dimensional inner solution at and near the free surface with the finite-element method. Coyle *et al.*

(1986) calculated the full two-dimensional flow field and quantified the limits of applicability of the asymptotic analysis.

The mechanism by which this flow becomes unstable can be grasped qualitatively from an argument that dates back to Pearson (1960) and Pitts & Greiller (1961). In the flow two major forces are in competition: capillary pressure arising from the action of surface tension in a curved meniscus; and a pressure force arising from the action of viscosity in a passage of slowly varying width, the well-known mechanism of hydrodynamic lubrication. Two dimensionless parameters pertain to the situation: the capillary number $Ca = \mu V/\sigma$ (μ is viscosity, V is roll surface speed, and σ is the surface tension), which measures the ratio of viscous and surface-tension forces, and the geometric factor H_0/R (H_0 is the half-gap width between two rolls of radius R), to which the slope between roll surfaces is proportional.

Saffman & Taylor (1958), in analysing the viscous fingering instability in displacement of liquid by gas between parallel walls (a Hele-Shaw cell), used a rectilinear flow approximation to show that the flow is unstable if the pressure gradient is greater in the fluid phase being displaced, as is always the case when the less viscous fluid displaces the more viscous (see Ruschak 1983). Pearson (1960) and Pitts & Greiller (1961), in analysing the ribbing instability of flows under wedge-spreaders and rollers, showed how a stabilizing influence of capillary pressure arises when the meniscus between liquid and gas is located between diverging walls: the meniscus becomes less curved when it shifts towards the gas, and vice versa. In addition, the diverging geometry modifies the destabilizing pressure gradient from its counterpart in the displacement flow of Hele-Shaw type. Lacking a set of boundary conditions for the film-splitting region, Pearson could determine neither the steady-state meniscus location nor the flow rate, and thus could not derive a specific stability criterion. Pitts & Greiller approximated the force balance at the perturbed meniscus to produce the intuitively appealing criterion that the flow becomes unstable if the pressure gradient in the liquid exceeds a certain value:

$$\frac{\mathrm{d}p}{\mathrm{d}x} > \frac{1}{Ca}\left[\frac{1}{r^2}\frac{\mathrm{d}r}{\mathrm{d}x} + N^2\right]. \tag{1}$$

Here r is the radius of curvature of the meniscus in the plane perpendicular to the roll axes, x is the primary flow direction (i.e. the direction of wall movement), p is the pressure, and N is the transverse wavenumber of the insipient ribbing represented as a sinusoidal perturbation. With numerous simplifying assumptions, they arrived at the stability criterion $Ca < 28\ (H_0/R)$. According to (1), surface tension is always a stabilizing influence, which is greater the higher the frequency of insipient ribbing (i.e. the shorter the wavelength). If the pressure gradient in the liquid is negative, i.e. pressure decreases in the downstream direction, the flow is always stable. If the pressure gradient is positive, the flow can be either stable or unstable, depending on the relative magnitude of the pressure gradient in the liquid and the variation of capillary pressure with meniscus location, which is proportional to surface tension and the local diverging angle of the roll surfaces.

Savage's (1977*b*, 1984) approach (see also Greener 1979 and Gokhale 1983*a*, *b*), in contrast to Pearson's classical linear stability analysis, was to search for necessary conditions for steady ribbing to be a solution to the equations of nearly rectilinear flow. They examined a number of *ad hoc* boundary conditions at the meniscus for the nearly rectilinear steady flow and the resulting stability criterion. The disturbing

feature of this work is that a prediction of the onset of instability in better accord with then-available data was obtained by using an inferior flow model. In particular, Savage's earlier work which gave poor predictions (see Greener 1979), used flow boundary conditions at a free surface that were proposed by Coyne & Elrod (1970) and later shown by Ruschak (1982) to be the best of the approximate models that have been used with lubrication theory.

The most acceptable analysis of ribbing to date is that of Ruschak (1983, 1985), who used the nearly rectilinear flow linear stability analysis of Pearson but applied boundary conditions derived from the results of his own solution to the asymptotic equations of two-dimensional flow near the meniscus. His predictions of ribbing onset compare well with published observations at small ratios of gap half-width to roll radius (H_0/R). The predictions cannot be expected to be accurate over the entire range of parameters for which observations have been published. The asymptotic approximations of the base flow lose accuracy as the gap widens or the capillary number falls. Moreover, the stability analysis loses accuracy as the wavenumber increases (high-frequency incipient ribbing).

Accurate predictions of stability require accurate theoretical analysis of both the base state and the response to three-dimensional disturbances of small amplitude. As Ruschak (1985) emphasized, simplifications in these analyses cast doubt on the validity of their results and in turn '...the ad-hoc boundary conditions become as much a subject of attention as the original problem'.

The later sections of this paper deal with the means and outcome of making accurate predictions. But first we address a related problem: How accurate are the observations of the 'onset of ribbing'?

2. Experimental determination of the onset of ribbing

The onset of ribbing in symmetric film-splitting was studied by Pitts & Greiller (1961), Mill & South (1967), Greener *et al.* (1980), and Benkreira, Edwards & Wilkinson (1982). All of these investigators relied on the unaided eye to detect the first appearance of ribbing. Their results are seemingly discordant: the critical capillary number as reported by the four respective groups is

$$Ca = 62\left(\frac{H_0}{R}\right)^1, \quad 17.3\left(\frac{H_0}{R}\right)^{\frac{3}{4}}, \quad 7500\left(\frac{H_0}{R}\right)^2, \quad 13.5\left(\frac{H_0}{R}\right)^{\frac{2}{3}}. \tag{2}$$

The most likely reason for the discrepancies lies in the subjective nature of discriminating between uniformity and non-uniformity of a small meniscus deep within the narrow gap between two cylinders. As the experimenter increases the roll speed (over a range of as much as a factor of 2 to 5) he sees a gradual transition from an apparently smooth (no curvature in the transverse direction) meniscus to a wavy one, but the waves that are first apparent are small in amplitude: moreover their wavelength is long compared to the gap width at the meniscus. That width is usually so small (50–250 μm) as to make it difficult to observe the meniscus itself, let alone any minute distortions along its length. Another possible source of discrepancies is that the rolls used by Benkreira *et al.* (1982) were mounted one above the other, rather than side-by-side, so that gravity did not act in the same direction and the upstream of the gap was not submerged in liquid as was the case in all the other experiments.

To establish a basis for comparison, we did experiments to determine the onset of

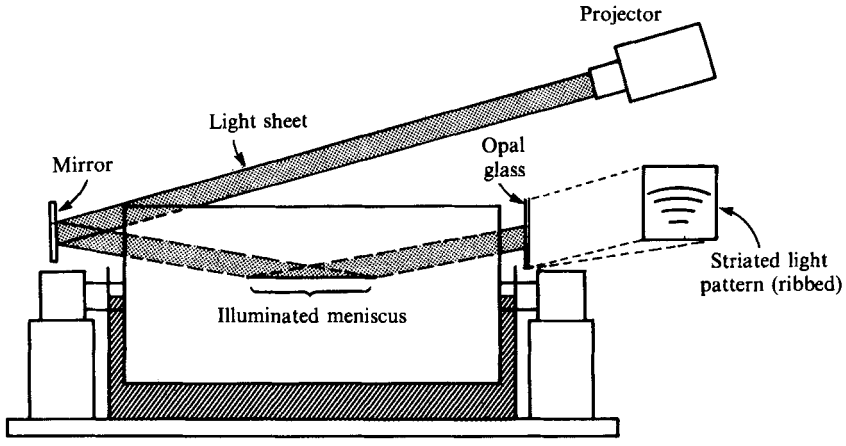

FIGURE 2. Schematic drawing of the experimental two-roll apparatus and the light-reflection system to detect small-amplitude ribs (side view).

ribbing by careful naked-eye viewing of the meniscus in much the same way as previous investigators. Then, in an attempt to resolve uncertainties, we tried various improved detection techniques and settled on one of much greater sensitivity, depicted in figure 2. A focused sheet of white light is produced by a 1 mm gap between the sharp edges of two razor blades fixed in a standard 35 mm slide mount. This light sheet, whose intersection with a plane is a narrow line segment, is reflected at a glancing angle off the meniscus between the cylinders. The light sheet travels parallel to the cylinder axis, strikes a 3–10 cm length of the meniscus, and is reflected onto a plate of opal glass. At low surface speeds of the cylinders, the image it makes is a curved patch of uniform intensity because the meniscus is uniform along its length. The image is not a line segment because the curvature of the meniscus perpendicular to the roll axis spreads the narrow sheet of light. At a certain higher speed the patch, as viewed by naked eye, distorts into alternating light and dark bands caused by a slight waviness of the meniscus. At this juncture the waviness itself cannot be detected with the naked eye. The speed is much less than reported by earlier investigators.

In this manner the critical capillary number at the onset of ribbing was measured for Newtonian glycerine/water solutions. Both 7.6 cm and 20.3 cm diameter roll pairs were used, each roll ground and mounted in bearings so that the total indicated runout (TIR) was less than 2.5 μm and driven at speed constant to within $\pm 0.25\%$. The roll pairs were 15.2 and 30.5 cm long, respectively. Viscosity was varied from 0.1 to 0.8 Pa s and the gap between the rolls ranged from 25 to 1250 μm. This gap range allowed overlap in the gap/diameter ratio (H_0/R) between measurements taken on the two different apparatus.

It should be noted that the chosen detection technique is still subjective because the light pattern must be viewed with the naked eye in order to judge the onset of ribbing. Its big advantage is that the light pattern is large and easy to observe, and the transition is sharp and dramatic. This makes the measurement simple, and choosing an incident light angle of only 10°–15° allows the detection of much smaller amplitude waves than is possible with naked-eye observations.

3. Stability analysis

The advent of computers and sophisticated computer-based schemes for solving partial differential equations has made it possible to analyse complicated fluid flows with considerable rigour. Finite-element analysis, as summarized by Kistler & Scriven (1983), has proved a powerful tool for predicting steady, viscous free-surface flows. Moreover, the stability of these flows can be predicted with linear stability theory combined with finite-element techniques developed by Ruschak (1983) and Bixler (1982). It is no longer necessary to use the lubrication approximation along with *ad hoc* boundary conditions.

3.1. *Formulation*

The first step in linear stability analysis is to perturb the steady-state flow with an infinitesimal disturbance. The disturbance is represented by Fourier modes in the transverse (z) direction; so the velocities, pressure, and free-surface parameters are written as

$$\boldsymbol{u}(x,y,z,t) = \boldsymbol{u}^0(x,y) + \epsilon \boldsymbol{u}'(x,y)\cdot\boldsymbol{D}(Nz)\,\mathrm{e}^{\beta t}, \tag{3}$$

$$p(x,y,z,t) = p^0(x,y) + \epsilon p'(x,y)\cos(Nz)\,\mathrm{e}^{\beta t}, \tag{4}$$

$$h(\xi,z,t) = h^0(\xi) + \epsilon h'(\xi)\cos(Nz)\,\mathrm{e}^{\beta t}, \tag{5}$$

where $\boldsymbol{D} = \cos(Nz)(\boldsymbol{ii}+\boldsymbol{jj}) + \sin(Nz)\boldsymbol{kk}$, N is the transverse wavenumber of the disturbance ($N = 2\pi H_0/\lambda$, λ is the wavelength) and β is its growth factor. The base flow (u^0, p^0, and h^0) is found by solving the equations of steady two-dimensional flow (see Coyle *et al.* 1986), and the x- and y-components of the disturbance are expanded in the same set of finite-element basis functions as used to represent the base flow.

The next step is to require that the three-dimensional unsteady flow field (3)–(5) satisfy the equations of motion throughout the domain sketched in figure 3:

$$Re\frac{\delta \boldsymbol{u}}{\delta t} = -Re\,\boldsymbol{u}\cdot\nabla\boldsymbol{u} + \nabla\cdot\boldsymbol{T} + St\boldsymbol{f}, \tag{6}$$

$$0 = \nabla\cdot\boldsymbol{u} \tag{7}$$

$$\boldsymbol{n}\cdot\frac{\delta \boldsymbol{x}}{\delta t} = \boldsymbol{n}\cdot\boldsymbol{u} \quad \text{(free surface)}. \tag{8}$$

Inertia, as indicated by the Reynolds number $Re = \rho V H_0/\mu$, and gravity, as indicated by the Stokes number $St = \rho g H_0^2/\mu V$, are included. For the cases of interest here, the unit vector $\boldsymbol{f}$ points in the negative x-direction (cf. figures 1, 3). $\boldsymbol{T}$ is the total stress tensor ($-p\boldsymbol{\delta} + \nabla\boldsymbol{u} + \nabla\boldsymbol{u}^{\mathrm{T}}$), $\boldsymbol{n}$ is the unit normal vector of the free surface, and $\boldsymbol{x}$ is the position of the free surface. Galerkin weighted residuals are formed using the basis functions $\phi^i(x,y)\boldsymbol{D}(Nz)$ as the weighting functions. Each weighted residual of the momentum equation is integrated by parts using the divergence theorem. The domain of integration (see figure 3) is the two-dimensional flow domain extended over one wavelength in the z-direction. The expressions for the flow field (equations (3)–(5)) are inserted in the volume integral of the weighted residual and the result is linearized with respect to ϵ. In the resulting equations for the vanishing of each weighted residual, the only z-dependence that remains is in factors of $\cos^2(Nz)$ or $\sin^2(Nz)$, either of which integrates analytically to produce a common factor of $\frac{1}{2}\pi$. There is also a common factor of $\mathrm{e}^{\beta t}$.

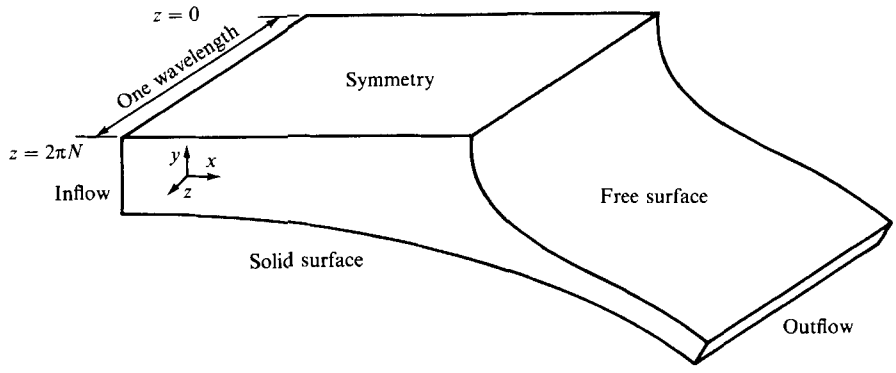

FIGURE 3. Definition sketch of the domain of the theoretical analysis, depicting various parts of its bounding surfaces.

Differentiating each of the equations with respect to the finite-element coefficients of the disturbance $(\boldsymbol{u}', p', h')$ results in the generalized asymmetric eigenproblem:

$$\beta \boldsymbol{M}\boldsymbol{q} = \boldsymbol{J}\boldsymbol{q}, \tag{9}$$

where $\boldsymbol{q}$ is the column vector of coefficients $[u', v', w', p', h']^{\mathrm{T}}$, $\boldsymbol{M}$ is a singular matrix of basis function overlaps (sometimes referred to as the mass matrix) arising from the time-dependence, and $\boldsymbol{J}$ is the Jacobian matrix.

The three basic parts of the Jacobian arise from the right-hand sides of the momentum equation (6), the continuity equation (7), and the kinematic equation (8). The structure of the Jacobian with all the entries summarized is given in the Appendix. Care is needed in deriving formulae for the Jacobian entries because the mapping of the elements underneath the free surfaces onto a fixed domain depends on the disturbance itself and therefore so too do quantities such as spatial derivatives and the Jacobian of the element mappings. Such quantities are obtained through the isoparametric map, the chain rule, and the mesh-generation algorithm used in a particular flow problem. Examination of the Appendix shows that most of the Jacobian matrix entries in the stability analysis are identical to those in the Jacobian formed in solving the base flow by Newton iteration. The only additional terms stem from T_{xz}, T_{yz}, and T_{zz}, terms that are zero in the base flow but not in the stability equations. These extra terms are proportional to either N or N^2.

The boundary integral $\int \boldsymbol{n}\cdot\boldsymbol{T}\,\mathrm{d}\Gamma$ in each equation for the vanishing of a momentum weighted residual has six distinct parts (see figure 3): (i) solid surfaces, (ii) edge boundaries (the planes $z = 0$ and $z = 2\pi/N$), (iii) symmetry planes, (iv) inflow boundaries, (v) outflow boundaries, and (vi) free surfaces. Boundary conditions of no slip and no penetration apply at solid surfaces, and because these are essential conditions they replace the weighted residual equations there. Because the domain width is chosen as one wavelength $(2\pi/N)$, the boundary integral over the edge boundaries drops out by virtue of cancellation of contributions from opposing edges. The boundary integral over the symmetry planes drops out because on them $\boldsymbol{n}\cdot\boldsymbol{T} = 0$. Inflow boundary conditions are either no perturbation in the velocities or no perturbation in the traction. Zero traction is imposed at the outflow plane.

The last remaining part of the boundary is the free surface, where the shear stress

is negligible and the normal stress must balance the capillary pressure, which is proportional to the surface tension and the mean curvature of the free surface:

$$\boldsymbol{n}\cdot\boldsymbol{T} = \frac{1}{Ca}(\nabla_{\mathrm{II}}\cdot\boldsymbol{n})\boldsymbol{n}. \tag{10}$$

Here the curvature of the surface is written as the surface divergence of the unit normal vector field, which in turn can be represented over the boundary of each element on the free surface in terms of the local isoparametric map. The surface divergence theorem (Weatherburn 1929) is used to reduce the order of the derivatives in the boundary integral, leading to the boundary condition that the slope of the disturbance approaches zero at the outflow of the computational domain. Here again, the Jacobian entries differ only in minor ways from those of the steady-flow calculation.

The mass matrix consists of two terms. The first arises from the momentum equations; it is proportional to Reynolds number and is detailed by Bixler (1982). It is not shown in the Appendix because it is negligible, and is dropped in an approximation that is discussed later. The other contribution to this matrix arises from the time-dependent portion of the kinematic boundary condition, (8). This boundary condition states that the velocity of the free surface (proportional to time derivatives of the free-surface parameters h) is equal to the velocity of the fluid underneath it (u, v, w). Because both sets of quantities are of order ϵ in the z-direction and dot products are being formed, the z-dimension enters first at $O(\epsilon^2)$ and only the two-dimensional forms need be considered.

3.2. *Solution*

Once the finite-element equations are constructed and the Jacobian and mass matrix are both evaluated, the generalized asymmetric eigenproblem must be solved for its eigenvalues, the exponential growth factors β_i, and its eigenvectors, their associated modes $\boldsymbol{q}_i$, all as functions of the transverse wavenumber N. Because the rank of $\boldsymbol{M}$ is typically on the order of 1000–6000 (the total number of momentum, continuity, and kinematic-weighted residual equations), special techniques are required. Bixler (1982) adapted a method developed by Stewart (1978) to compute the most dangerous subspace of eigenfunctions. An alternative to this iterative calculation of the dominant subspace of the complete eigenproblem is Ruschak's (1983) approach, which is adopted here. He neglected the time derivatives in the momentum equations, an approximation that is accurate if the timescale of the disturbance is long compared to that of the base flow. It is probably adequate here because the flows of interest have Reynolds numbers less than 0.001. Furthermore, if the instability of interest is not oscillatory in time, then the imaginary part of the eigenvalue is zero. Then through the condition of neutral stability the real part too is zero, and so a zero multiplies $\boldsymbol{M}$ in (8). Thus the calculation of marginal stability is completely independent of any approximations used in evaluating $\boldsymbol{M}$, no matter how large the Reynolds number is. The only time derivatives that remain arise from the kinematic boundary condition; thus the dimension of the eigenproblem is reduced to the order of 10–100 and standard algorithms for solving small eigenproblems can be used. This makes the cost of the eigenproblem solution less than 10% of the total computer time.

3.3. *Computation*

Initial computations on a coarse mesh were done on a Cray-1 computer, final results on an IBM 3081 computer. Gauss elimination was performed by a modified version

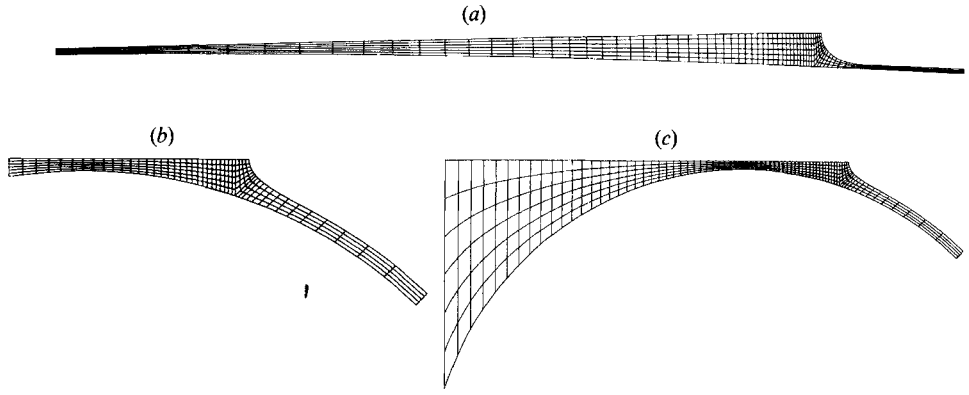

FIGURE 4. Finite-element discretizations used in calculating the stability of two-dimensional symmetric film-splitting to ribbing at (*a*) $H_0/R = 0.000\,125$, (*b*) $H_0/R = 0.025$, and (*c*) $H_0/R = 0.025$ with extended upstream region.

of Hood's (1976) frontal solver, while eigenvalues and eigenvectors were calculated by the IMSL routine 'EIGZF'. Computations of the steady two-dimensional base flows typically took 60 cpu s and 3 megabytes of memory (*ca.* 3900 unknowns, 3 Newton iterations to converge). Computation of the stability of the base flow at one wavenumber typically took 45 c.p.u.s and 6 megabytes of memory (*ca.* 5600 unknowns, 45 eigenpairs).

For each set of parameters ($H_0/R, Re, Ca, St$), eigenvalues were computed over a range of wavenumbers to see if any of them had positive real part, i.e. corresponded to an unstable mode. For a given H_0/R (fixed gap), the eigenvalue of the most dangerous mode was plotted against wavenumber with Ca as a parameter. Most dangerous mode refers to that eigenfunction whose eigenvalue has the largest real part and thus would have the fastest exponential growth rate (or the slowest decay rate). For the film-splitting problem, the most dangerous modes were always real.

4. Results and discussion

The results were obtained with discretizations such as are shown in figure 4. The sensitivity of base flows and eigenvalues to the refinement of the discretization were tested by repeating the computations with more elements and by moving the location of the upstream boundary further upstream. The refinement shown in figure 4(*a*, *b*) was sufficient to determine the critical capillary number and wavenumber both to within at least 1%. Figure 4(*c*) is an example of a mesh extended far upstream to ensure the same insensitivity of the results to the location of the inlet boundary.

4.1. *Stability of the most dangerous mode*

The computed eigenvalue of the most dangerous mode as a function of capillary number and gap/diameter ratio is shown in figure 5. At low capillary numbers, the base flow is stable to all modes, but at high capillary numbers, there are unstable modes of non-zero wavenumber. At an intermediate capillary number, the curve of eigenvalue versus wavenumber is tangent to the x-axis, the condition that defines the critical capillary number and wavenumber at the onset of ribbing. The results show that at narrower gaps between the rolls the flow becomes unstable at lower capillary number, and to transverse standing waves, or ribs, that are long compared to the gap

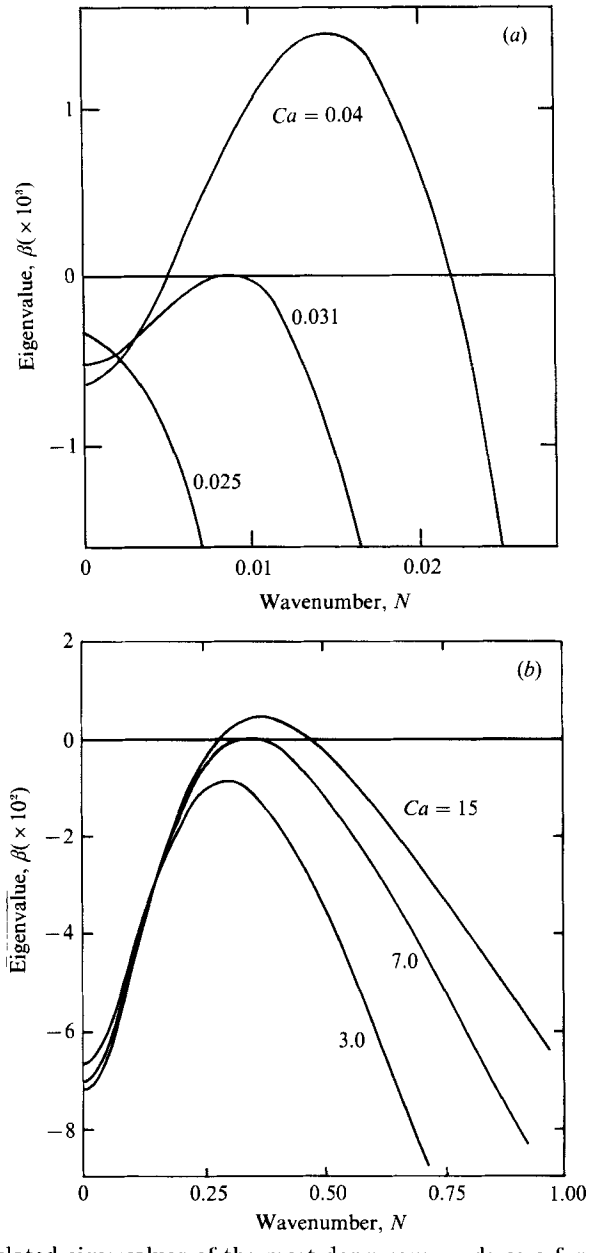

FIGURE 5. Calculated eigenvalues of the most dangerous mode as a function of wavenumber and capillary number at (*a*) $H_0/R = 0.000125$, and (*b*) $H_0/R = 0.025$ ($Re = St = 0$).

(i.e. the narrower the gap, the smaller is N). The free-surface component of one such mode is shown in figure 6, along with the disturbed flow pattern near the free surface. The sinusoidal disturbance is greatest near the symmetry plane and decays rapidly downstream. Each rib contains a pair of vortices in which liquid rotates such that the flow wells up to the free surface under the crest of the rib and descends under the trough. Except at the symmetry plane, there is a strong downstream velocity component superimposed on the circulatory flow: consequently fluid elements move downstream in helical trajectories under the ribs.

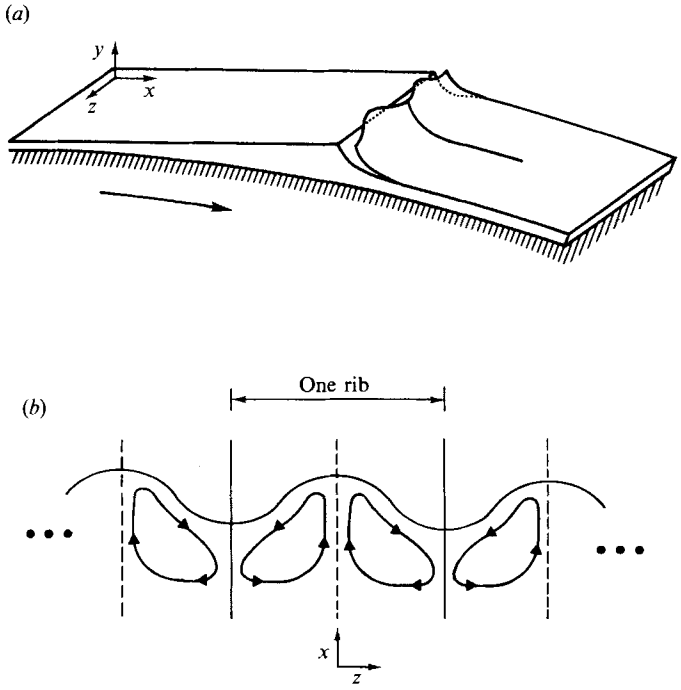

FIGURE 6. Calculated eigenvector of the most dangerous mode at the neutral stability point (onset of ribbing) at $H_0/R = 0.005$ ($Re = St = 0$).

H_0/R	Ca	N	λ/H_0	λ/R	α
0.000125	0.031	0.0087	722	0.090	6.3
0.000333	0.050	0.016	393	0.131	8.8
0.001	0.094	0.034	185	0.185	12.9
0.002	0.150	0.055	114	0.228	16.3
0.005	0.32	0.105	60	0.299	22.2
0.0125	0.96	0.20	31	0.393	30.2
0.020	2.7	0.29	22	0.433	35.8
0.025	7.0	0.34	18	0.462	39.2

TABLE 1. Critical conditions for the onset of ribbing as computed by finite-element-based linear stability theory

The plots of the eigenvalue of the most dangerous mode β *vs.* the transverse wavenumber N can be used to determine the critical capillary number for the onset of ribbing at several gap/diameter ratios (H_0/R), as recorded in table 1. The diverging angle α between the roll surfaces at the point where the meniscus forms is also recorded. As discussed by Ruschak (1985), increasing α stabilizes the flow with respect to ribbing, resulting in much higher values of the critical capillary number.

The effect of gravity, acting in the direction from the meniscus towards the gap (figure 1), is to stabilize the flow. The relevant dimensionless group is the Stokes number, which can be arranged into the form

$$St = \left(\frac{\rho g R^2}{\sigma}\right)\frac{(H_0/R)^2}{Ca}. \tag{11}$$

The results of calculations at two values of gap/diameter ratio are reported in table

H_0/R	St	Ca	α	N	λ/H_0
0.000125	0	0.031	6.32	0.0087	722
0.000125	0.001	0.031	6.33	—	—
0.000125	0.001	0.033	6.22	0.0091	690
0.005	0	0.32	22.2	0.105	60
0.005	0.05	0.32	22.7	—	—
0.005	0.05	0.83	19.8	0.15	42

TABLE 2. Effect of gravity on computed steady flows and critical conditions for the onset of ribbing ($Re = 0$)

H_0/R	Re	Ca	α	N	λ/H_0
0.000125	0	0.031	6.32	0.0087	722
0.000125	1	0.031	6.40	—	—
0.000125	1	0.029	6.52	0.0084	748
0.005	0	0.32	22.1	0.104	60
0.005	1	0.32	23.0	—	—
0.005	1	0.345	22.7	0.100	63

TABLE 3. Effect of inertia on computed steady flows and critical conditions for the onset of ribbing ($St = 0$)

2, where values of St are approximately 5–10 times those typical for our experiments. Increasing the Stokes number causes the meniscus to move farther out of the gap, increasing α and thus apparently stabilizing the flow field, but the magnitude of this change is small. This same increase in St results in a significant stabilization of the flow as measured by the marked increase in the critical capillary number. This indicates that the primary influence of gravity enters through the perturbation equations rather than by simply shifting the steady-state meniscus position.

The effect of inertia, as measured by the Reynolds number,

$$Re = \left(\frac{\rho R\sigma}{\mu^2}\right)\left(\frac{H_0}{R}\right)Ca, \tag{12}$$

is more complex. Results of calculations at $Re = 1$ are reported in table 3; values of $Re < 0.01$ are typical in our experiments with relatively viscous liquids. Increasing the Reynolds number causes the meniscus to relocate to a point of larger α, thus apparently stabilizing the flow field. But the primary effect of inertia is to stabilize short-wavelength disturbances and to destabilize long-wavelength ones. (Here the length is measured relative to the gap: see table 3.) At large gaps the shorter waves correspond to the most dangerous modes and so the flow is *stabilized* with respect to ribbing. Conversely, at small gaps the longer waves correspond to the most dangerous modes and so the flow is *destabilized*. Thus the effect of inertia on the stability of the flow depends, through the perturbation equations, upon the wavelength of the most dangerous mode. The magnitude of this effect is small, so that it might only be observed in experiments with liquids of viscosity less than 0.1 Pa s.

The effects of inertia and gravity are interesting and could be significant under certain experimental conditions. Both are insignificant at the conditions of the experiments with which we wish to compare our theory, and so are not considered further.

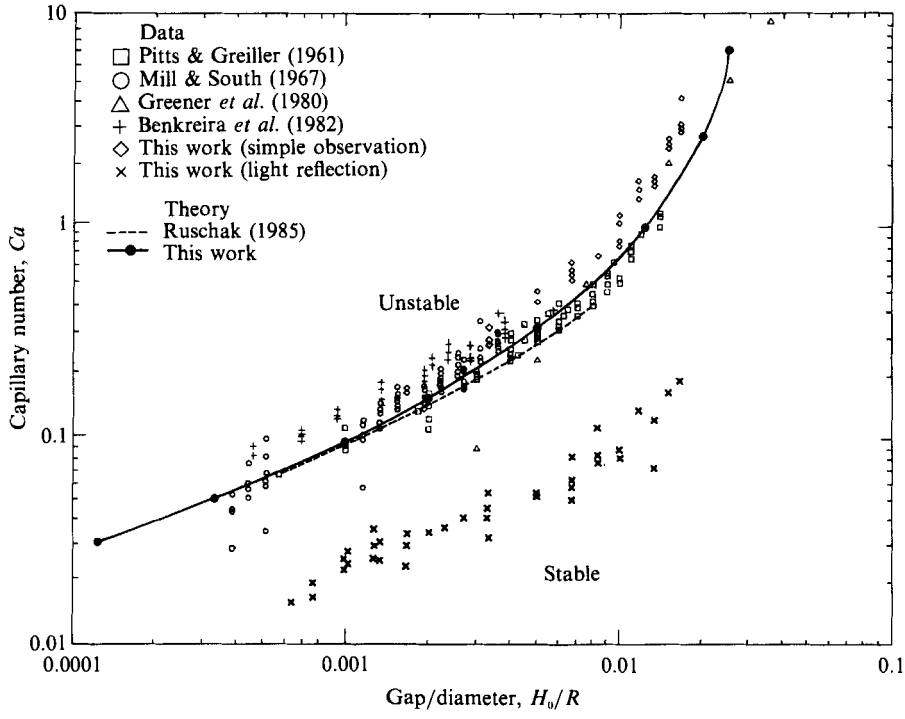

FIGURE 7. Critical capillary number for the onset of ribbing as a function of the gap/diameter ratio ($Re = St = 0$).

4.2. *Comparison with previous theory and experiment*

This full theoretical analysis of the onset of ribbing predicts that the flow is more stable to ribbing than had previously been estimated by means of lubrication theory (see Pitts & Greiller 1961; Greener *et al.* 1980). As shown in figure 7, Ruschak's (1985) analysis, reviewed above, predicts a stability limit only slightly lower than the current analysis, with the two theoretical results becoming indistinguishable at small gaps ($H_0/R < 0.001$). The reason is that at the film-split meniscus location the diverging angle of the roll surfaces (table 1) is small enough that the rectilinear flow approximations used by Ruschak in both steady flow and stability analyses are accurate. Even where the diverging angle is not small, the asymptotic analysis predicts critical capillary numbers which are within 20% of those predicted by the full theory.

In figure 7 are also plotted all previously published naked-eye measurements of the onset of ribbing. Plainly the values of the critical capillary number reported by all investigators, including ourselves, scatter yet agree within the experimental uncertainty. Examining the data in this manner, rather than by simply comparing published curves fitting the data, leads to the conclusion that the measurements of the previous investigators were never in disagreement. With the exception of four stray points, a continuous curved band of data points extends from $H_0/R = 0.0004$ to $H_0/R = 0.035$, and the slope of this band rises from $\frac{1}{2}$ at small gaps to about 2 or 3 at large gaps. Furthermore, the theoretically predicted curve passes through the middle of this band for the entire two orders of magnitude of gap/diameter ratio.

Figure 8 shows the wavelength of the ribbing disturbance as a function of gap/diameter ratio H_0/R. The prediction is in agreement with experimental results

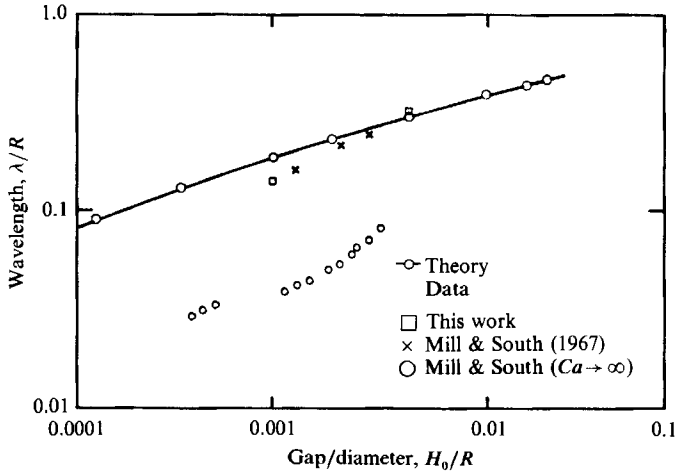

FIGURE 8. Critical wavelength at the onset of ribbing as a function of the gap/diameter ratio ($Re = St = 0$).

of Mill & South (1967) and the current work. The wavelength at the onset of ribbing can be a significant fraction of the roll radius: it varies from 10% at small gap to 50% at large gap. Because the length of the rolls used in the various experimental apparatuses ranged from 2–8 times the roll radius, at the onset of ribbing the wavelength of the ribs is a significant fraction of the roll length. Near the onset, the wavelength shortens rapidly as the capillary number increases. This is in contrast to the high-capillary-number regime, where the capillary number is at least 2.5 times the critical value and the wavelength is no longer sensitive to changes in the capillary number. As shown in figure 8, here wavelengths are generally 5 times shorter than at the onset and are thus small compared to both the roll radius and length.

The critical capillary number measured in the new experiments using the glancing angle reflection of a sheet of light off of the meniscus are shown alongside all other results in figure 7. This technique is capable of detecting much smaller amplitude waves on the meniscus than can be detected by the usual naked-eye observations. The amplitude of these waves is estimated to be on the order of 5 μm, based on calculation of the amplitude of a sinusoidal wave on the meniscus that would deflect a light ray striking the opal glass by 1–5 mm. The results of these measurements indicate that the more sensitive the observation technique, the lower the measured value of the critical capillary number. Critical capillary numbers measured in this manner are roughly a factor of five lower than those measured with the naked eye. Experimental observations indicate that at these low capillary numbers the amplitude of the waves is small (~ 5 μm) and increases very slowly with increasing capillary number. At capillary numbers near the apparent onset of ribbing as determined by the naked eye the amplitude becomes large enough for the waves to be plainly visible and becomes very sensitive to the capillary number. The light pattern at low capillary number is steady, indicating that a standing wave pattern is being observed and the observations are not an artifact introduced by mechanical vibrations or roll runout. The opal glass can be removed and the meniscus viewed with the naked eye at low angle. With this intense low-angle focused illumination, several wave crests are visible as regularly spaced bright spots along the illuminated section of the meniscus. These waves are not otherwise visible.

4.3. *The nature of the instability*

All of these observations and their relation to the theoretical predictions indicate that the instability is an 'imperfect' or 'perturbed' bifurcation (cf. Iooss & Joseph 1980; Keener & Keller 1973). The theoretical predictions are of onset of instability of a two-dimensional base flow, the onset marking bifurcation to a three-dimensional ribbed state. The base flow in the experiments is not two-dimensional, however. The rolls have ends.

At the roll ends the free surface of the liquid bends into a three-dimensional shape that joins the edges of the two liquid films that the rolls carry away from the film-split zone, the meniscus at the film-split, and the edge of the liquid carried into and through the gap between rolls. This last edge is a meniscus that widens into the free surface of the liquid beneath, in the pool in which the two rolls are half-submerged (obscured from view in figure 1). The three-dimensional shape at each roll end is such that the part of it between the rolls has the form of a standing wave from which emanates a rib in each film, i.e. a thickening of each film near its edge. The rib is made evident by a highlight in the photograph, figure 9(*a*), which is of one end of the two-roll apparatus operating at the relatively low capillary number ($\mu V/\sigma$) of 0.25. As the capillary number is increased, in this case by raising the roll speed, the rib grows sharper and thicker (figure 9*b*), and a second rib grows alongside it to detectable amplitude. As the capillary number is increased further, a whole family of ribs comes into view, as pictured in figure 9(*c*). The rib at the roll end is invariably the thickest, and the amplitudes of the others fall off with distance from the nearest roll end. Of course the roll speed or capillary number at which each successive rib becomes detectable depends strongly on the illumination and magnification employed, as detailed above.

Thus the base flow is made three-dimensional by the end effect. The evidence is that end ribs are always present in the base flow and are members of a whole family of ribs whose amplitude at low capillary number falls off so rapidly with distance from the end that they are too faint to detect. Near the capillary number at which theory predicts that a two-dimensional base flow would turn unstable and bifurcate to a ribbed state, the whole family of already existing ribs grow rapidly in amplitude as the capillary number is raised just a little. Moreover, when the capillary number is lowered, the ribs diminish in amplitude over the same capillary-number range. There is no discernible hysteresis: the transition though not abrupt seems reversible.

To predict quantitatively the details of the imperfect bifurcation would require solving the fully three-dimensional steady flow problem of which (6)–(8) are the chief equations. Doing so was beyond the scope of this research. An idea of the details can be drawn from experimental and theoretical analysis of an analogous flow, however.

The analogy is circular Couette flow in the annulus between concentric cylinders, the inner of which is rotated (Taylor 1923). Taylor's early stability analysis pertained to the axisymmetric, two-dimensional flow that infinitely long cylinders would allow, and subsequent theoretical work established that the onset of instability marks a supercritical, or 'soft', bifurcation from circular flow to Taylor's vortices at the critical Taylor number (cf. Kogelman & DiPrima 1970). But in painstakingly careful experiments, Coles (1965) observed the gradual appearance of Taylor vortices as the Taylor number was raised, those at the ends of his apparatus being the first to become detectable at the resolution he achieved, so that base flow in reality is weakly three-dimensional.

Benjamin (1978) explored at length the relevance of the theory of imperfect

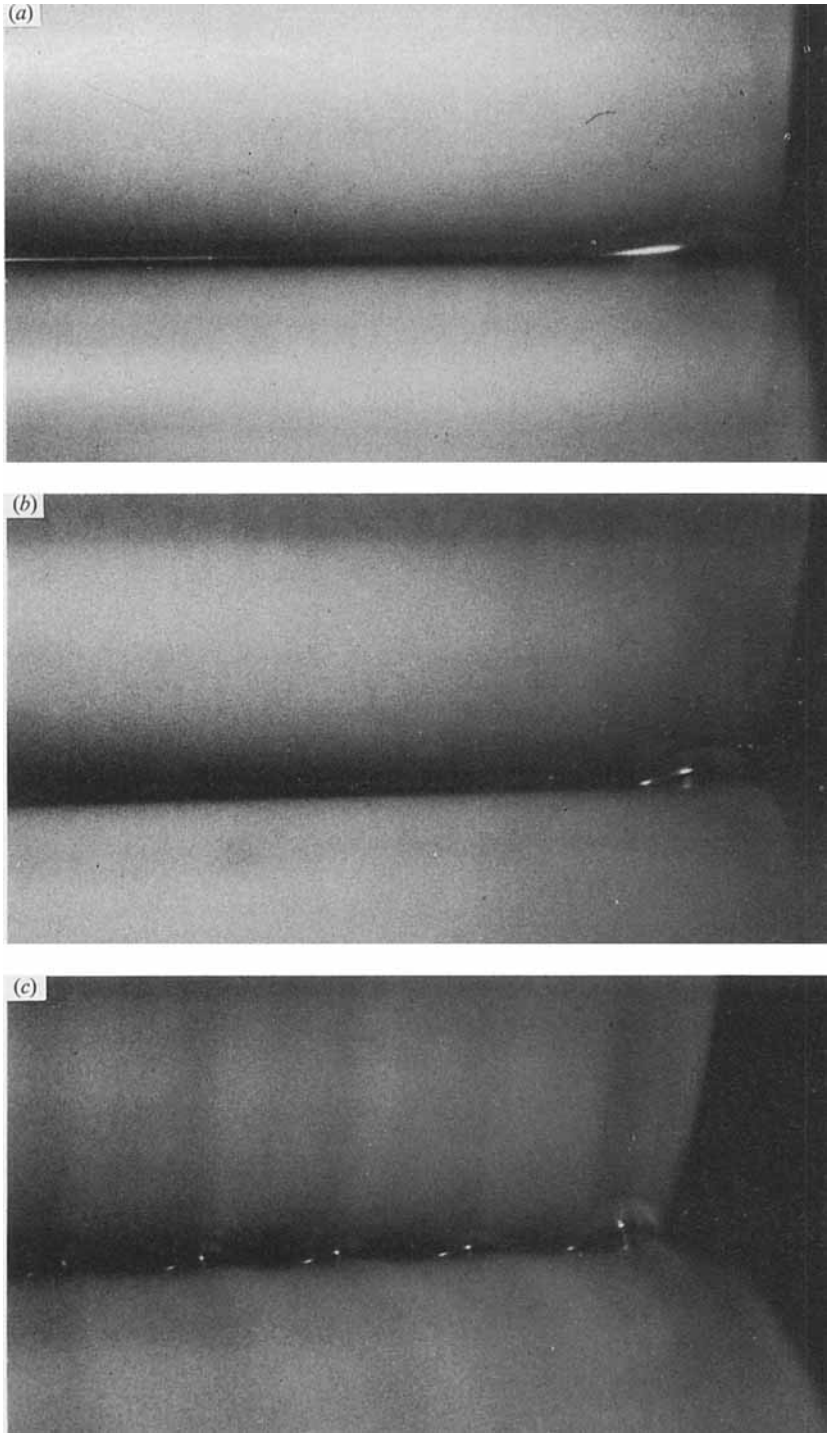

FIGURE 9. Photographs of the end waves present on the experimental apparatus which propagate towards the gap centre region even at low capillary number: $H_0/R = 0.005$; (*a*) $Ca = 0.25$, (*b*) $Ca = 0.4$, (*c*) $Ca = 0.5$.

bifurcation to these observations and further ones that Coles made. Among other findings that may also be pertinent to ribbing in film-splitting, there are three main points. First, the appearance of cells is a smooth process as the Taylor number is increased; there is no precise critical value below which cells are absent and above which cells appear. If the annulus is sufficiently long to include many cellular wavelengths the development of cells is rapid over a narrow range of Taylor number close to the theoretical critical value. Second, there can be hysteresis in the critical range and in the number of vortices at certain lengths of the apparatus, again when the apparatus is short enough. Third, at Taylor numbers substantially greater than the critical range the end effects can spawn a great multiplicity of flow states, e.g. metastable steady states with different numbers of vortices arrayed in the fixed length of the apparatus (Benjamin & Mullin 1981).

By analogy similar phenomena can be expected to accompany ribbing in film-splitting. Most significant is the virtual certainty that when the rolls are shorter than about ten times the wavelength of the ribs that would appear between infinitely long rolls, the wavelengths and growth with capillary number of the ribs actually present will be sensitive to roll length. The experiments reported above were conducted in an apparatus whose rolls proved to be about ten times the wavelength of the ribs that appeared in most instances. So the results probably apply to film-splitting between longer rolls. Another significant point in this analogy is that a multiplicity of flow states, some of them time-dependent, are observed at capillary numbers substantially higher than the critical value. These flow states correspond to varying numbers of ribs attempting to fit along the fixed length of the apparatus.

A further likelihood is that the influence of the end effect on the imperfect bifurcation to ribbing – the degree of imperfection, so to say – can be lessened by altering conditions at the roll ends. Certainly the edge meniscus can be virtually eliminated by installing end dams, plates or wedges mounted perpendicular to the roll axes near the roll ends to eliminate transverse flow off the ends of the rolls. The amplitude of the standing wave near each end of the roll might also be reduced by locally interferring upstream of it, that is by reducing and redistributing the flow carried into the gap behind it. These measures were not tested carefully in this work.

5. Summary

Symmetric film-splitting of Newtonian liquid between half-submerged cylinders of the same radius, counter-rotating at equal speeds, is a seemingly two-dimensional steady flow below a certain critical range of cylinder surface velocity, given the radius and separation of the cylinders, the viscosity, surface tension, and density of the liquid. However, the flow is distinctly three-dimensional at the ends of the cylinders, or rolls.

The three-dimensionality of the flow is first manifested, as the rolls are speeded up, in a single detectable rib at each end of the rolls. As the speed approaches the critical range, more and more of a family of ribs between the two ends grow to detectable amplitude. What is detectable depends strongly on the means of illuminating, magnifying, and viewing the film-splitting meniscus deep within the narrow gap between the rolls. In the critical range of roll speed the interior members of the family approach uniformity of amplitude and their amplitude rises sharply with roll speed. This is the onset of practically important ribbing. As the rolls are slowed down, the amplitude of the ribs falls equally sharply in the critical range: there is no discernible hysteresis.

Theoretical analysis brings out that the governing parameters are the capillary number, i.e. roll surface velocity times liquid viscosity divided by the liquid's surface tension; the ratio of gap to roll diameter; and secondarily a Reynolds number that measures the relevance of liquid inertia and a Stokes number that measures the effect of gravity on the viscous free-surface flow. Though the flow is three-dimensional, such analysis is formidable. It is efficient to analyse first the two-dimensional flow as if there were no end effects, and then to analyse the stability of that base flow to ribbing, or bifurcation to a three-dimensional state.

The pertinent Navier–Stokes systems of equations for both the base flow and its stability are solved via finite-element analysis. The solutions yield predictions of a critical capillary number at which the two-dimensional flow of smooth film-splitting becomes unstable with respect to a particular wavelength of ribbing. Ruschak's earlier predictions by means of an approximate analysis prove very close, except when the ratio of gap to roll diameter climbs past 0.01. The predicted critical capillary number falls within the critical range of capillary number in which the transition to easily detectable ribs has been observed in experiments.

The relationship of the three-dimensional reality as revealed by the new observations to the theoretical predictions indicates that the bifurcation is imperfect and is made so by the end effect, much in the same manner as the onset of Taylor cells in circular Couette flow. In other words, the base flow is inherently three-dimensional and ribbed, although below the critical range of capillary number the amplitude of ribbing may be so small as to be unimportant, or imperceptible, or even totally undetectable because it is masked by the effects of other small perturbing influences (e.g. roll runout or vibration). Nevertheless, there are aspects of the flow field, such as flow rate and average film thickness, pressure distribution, and average meniscus location, that can be accurately modelled as two-dimensional, even if the capillary number is above the critical range. Moreover, the critical range of capillary number can be usefully estimated from the theoretically predicted instability of strictly two-dimensional flow, since the small-amplitude ribs detected below this range would probably not be discernible on a finished coated product.

To conclude, there evidently is no precisely definable loss of stability, or onset of ribbing, in symmetric film-splitting between counter-rotating cylinders of finite length. From the standpoint of science the issue is one of three-dimensional effects in viscous free-surface flow, and stands as a challenge to theory and physical understanding. From the standpoint of practical applications the issue is what amplitude of ribbing is tolerable and how can design and operating conditions be chosen so that amplitude is not exceeded while other desired process objectives are achieved.

Further understanding of the precise nature of the ribbing instability will require much more sophisticated computation and experiment than presented here. A highly accurate quantitative measurement of the complete free-surface profile in this flow is necessary. Future computations need to be fully three-dimensional in order to accurately incorporate these important end effects. Owing to advances in computer technology, such computations are now becoming feasible.

The authors are indebted to K. J. Ruschak, S. F. Kistler and N. E. Bixler for many helpful discussions. Special thanks are due to K. N. Christodoulou for correcting an elusive error in the derivation of the finite-element equations. R. D. Baune assisted with much of the experimental work. This work was supported by the

3M Company. Computer time was supplied by the University of Minnesota Computer Center and the General Electric Company.

Appendix

The following is a summary of the asymmetric eigenproblem. The notation assumes 9-node quadrilateral elements with mixed interpolation, where ϕ^i are biquadratic basis functions for the representation of velocities and the isoparametric map, and ψ^i are bilinear basis functions for the representation of the pressure. Element nodes are numbered such that nodes 3, 6, 9 define the free surface ($\eta = 1$, when present). Superscripts run from 1 to 9 for momentum equations, 1 to 4 for continuity equations, and 1 to 3 for kinematic equations. Subscripts run from 1 to 9 for velocity derivatives, 1 to 4 for pressure derivatives, and 1 to 3 for free surface derivatives.

The generalized asymmetric eigenproblem can be written as

$$\beta \boldsymbol{M}\boldsymbol{q} = \boldsymbol{J}\boldsymbol{q}, \tag{A 1}$$

where $\boldsymbol{q}$ is the column vector $[u', v', w', p', h']^{\mathrm{T}}$, $\boldsymbol{M}$ is the mass matrix

$$\boldsymbol{M} = \begin{bmatrix} 0 & 0 & 0 & 0 & 0 \\ 0 & 0 & 0 & 0 & 0 \\ 0 & 0 & 0 & 0 & 0 \\ 0 & 0 & 0 & 0 & 0 \\ 0 & 0 & 0 & 0 & M^k_{ij} \end{bmatrix}, \tag{A 2}$$

and $\boldsymbol{J}$ is the Jacobian matrix

$$\boldsymbol{J} = \begin{bmatrix} \dfrac{\partial R^i_{mx}}{\partial u'_j} & \dfrac{\partial R^i_{mx}}{\partial v'_j} & \dfrac{\partial R^i_{mx}}{\partial w'_j} & \dfrac{\partial R^i_{mx}}{\partial p'_j} & \dfrac{\partial R^i_{mx}}{\partial h'_j} \\ \dfrac{\partial R^i_{my}}{\partial u'_j} & \dfrac{\partial R^i_{my}}{\partial v'_j} & \dfrac{\partial R^i_{my}}{\partial w'_j} & \dfrac{\partial R^i_{my}}{\partial p'_j} & \dfrac{\partial R^i_{my}}{\partial h'_j} \\ \dfrac{\partial R^i_{mz}}{\partial u'_j} & \dfrac{\partial R^i_{mz}}{\partial v'_j} & \dfrac{\partial R^i_{mz}}{\partial w'_j} & \dfrac{\partial R^i_{mz}}{\partial p'_j} & \dfrac{\partial R^i_{mz}}{\partial h'_j} \\ \dfrac{\partial R^i_{c}}{\partial u'_j} & \dfrac{\partial R^i_{c}}{\partial v'_j} & \dfrac{\partial R^i_{c}}{\partial w'_j} & 0 & \dfrac{\partial R^i_{c}}{\partial h'_j} \\ \dfrac{\partial R^i_{k}}{\partial u'_j} & \dfrac{\partial R^i_{k}}{\partial v'_j} & 0 & 0 & \dfrac{\partial R^i_{k}}{\partial h'_j} \end{bmatrix}. \tag{A 3}$$

The lone 3×3 mass matrix contribution from each element under the free surface arises from the kinematic equation integrated over the free surface:

$$M^k_{ij} = \int \left(-y_\xi \frac{\partial x_{3j}}{\partial h_j} + x_\xi \frac{\partial y_{3j}}{\partial h_j} \right) \phi^{3i} \phi^{3j} \, \mathrm{d}\xi. \tag{A 4}$$

The Jacobian matrix has many terms. They are summarized below.

Kinematic equation

$$\frac{\partial R_k^i}{\partial u_{3j}'} = \int -y_\xi \phi^{3i}\phi^{3j}\,\mathrm{d}\xi, \quad \frac{\partial R_k^i}{\partial v_{3j}'} = \int x_\xi \phi^{3i}\phi^{3j}\,\mathrm{d}\xi, \tag{A 5), (A 6}$$

$$\frac{\partial R_k^i}{\partial h_j'} = \int\left(-u\frac{\partial y_\xi}{\partial h_j} + v\frac{\partial x_\xi}{\partial h_j}\right)\phi^{3i}\,\mathrm{d}\xi. \tag{A 7}$$

Continuity equation

$$\frac{\partial R_c^i}{\partial u_j'} = \iint \psi^i \phi_x^j |J|\,\mathrm{d}\xi\,\mathrm{d}\eta, \quad \frac{\partial R_c^i}{\partial v_j'} = \iint \psi^i \phi_y^j |J|\,\mathrm{d}\xi\,\mathrm{d}\eta, \tag{A 8), (A 9}$$

$$\frac{\partial R_c^i}{\partial w_j'} = N\iint \psi^i \phi^j |J|\,\mathrm{d}\xi\,\mathrm{d}\eta, \tag{A 10}$$

$$\frac{\partial R_c^i}{\partial h_j'} = \iint\left(u_\xi\frac{\partial y_\eta}{\partial h_j} - u_\eta\frac{\partial y_\xi}{\partial h_j} - v_\xi\frac{\partial x_\eta}{\partial h_j} + v_\eta\frac{\partial x_\xi}{\partial h_j}\right)\psi^i\,\mathrm{d}\xi\,\mathrm{d}\eta. \tag{A 11}$$

x-momentum equation

$$\frac{\partial R_{mx}^i}{\partial u_j'} = \iint [2\phi_x^i\phi_x^j + \phi_y^i\phi_y^j + N^2\phi^i\phi^j + Re\,\phi^i(u_x\phi^j + u\phi_x^j + v\phi_y^j)]|J|\,\mathrm{d}\xi\,\mathrm{d}\eta \tag{A 12}$$

$$\frac{\partial R_{mx}^i}{\partial v_j'} = \iint [\phi_y^i\phi_x^j + Re\,u_y\phi^i\phi^j]|J|\,\mathrm{d}\xi\,\mathrm{d}\eta \tag{A 13}$$

$$\frac{\partial R_{mx}^i}{\partial w_j'} = -N\iint \phi^i\phi_x^j|J|\,\mathrm{d}\xi\,\mathrm{d}\eta, \quad \frac{\partial R_{mx}^i}{\partial p_j'} = -\iint \phi_x^i\psi^j|J|\,\mathrm{d}\xi\,\mathrm{d}\eta. \tag{A 14), (A 15}$$

y-momentum equation

$$\frac{\partial R_{my}^i}{\partial u_j'} = \iint [\phi_x^i\phi_y^j + Re\,v_x\phi^i\phi^j]|J|\,\mathrm{d}\xi\,\mathrm{d}\eta, \tag{A 16}$$

$$\frac{\partial R_{my}^i}{\partial v_j'} = \iint [\phi_x^i\phi_x^j + 2\phi_y^i\phi_y^j + N^2\phi^i\phi^j + Re\,\phi^i(v_y\phi^j + u\phi_x^j + v\phi_y^j)]|J|\,\mathrm{d}\xi\,\mathrm{d}\eta, \tag{A 17}$$

$$\frac{\partial R_{my}^i}{\partial w_j'} = -N\iint \phi^i\phi_y^j|J|\,\mathrm{d}\xi\,\mathrm{d}\eta, \quad \frac{\partial R_{my}^i}{\partial p_j'} = -\iint \phi_y^i\psi^j|J|\,\mathrm{d}\xi\,\mathrm{d}\eta. \tag{A 18), (A 19}$$

z-momentum equation

$$\frac{\partial R_{mz}^i}{\partial u_j'} = -N\iint \phi_x^i\phi^j|J|\,\mathrm{d}\xi\,\mathrm{d}\eta, \quad \frac{\partial R_{mz}^i}{\partial v_j'} = -N\iint \phi_y^i\phi^j|J|\,\mathrm{d}\xi\,\mathrm{d}\eta, \tag{A 20), (A 21}$$

$$\frac{\partial R_{mz}^i}{\partial w_j'} = \iint [\phi_x^i\phi_x^j + \phi_y^i\phi_y^j + 2N^2\phi^i\phi^j + Re\,\phi^i(u\phi_x^j + v\phi_y^j)]|J|\,\mathrm{d}\xi\,\mathrm{d}\eta, \tag{A 22}$$

$$\frac{\partial R_{mz}^i}{\partial p_j'} = -N\iint \phi^i\psi^j|J|\,\mathrm{d}\xi\,\mathrm{d}\eta. \tag{A 23}$$

Momentum equations – free-surface derivatives

$$\frac{\partial R^i_{mx}}{\partial h'_j} = \iint\Big[(-p+2u_x)\frac{\partial \phi^i_x|J|}{\partial h_j}+(u_y+v_x)\frac{\partial \phi^i_y|J|}{\partial h_j}+2\phi^i_x\frac{\partial T_{xx}}{\partial h_j}+\phi^i_y\frac{\partial T_{xy}}{\partial h_j}$$
$$+Re\,\phi^i u\Big(u_\xi\frac{\partial y_\eta}{\partial h_j}-u_\eta\frac{\partial y_\xi}{\partial h_j}\Big)+Re\,\phi^i v\Big(-u_\xi\frac{\partial x_\eta}{\partial h_j}+u_\eta\frac{\partial x_\xi}{\partial h_j}\Big)$$
$$+St\,\phi^i\frac{\partial|J|}{\partial h_j}-N^2\Big(u_x\frac{\partial x}{\partial h_j}+u_y\frac{\partial y}{\partial h_j}\Big)\phi^i|J|\Big]\,\mathrm{d}\xi\,\mathrm{d}\eta, \tag{A 24}$$

$$\frac{\partial R^i_{my}}{\partial h'_j} = \iint\Big[(u_y+v_x)\frac{\partial \phi^i_x|J|}{\partial h_j}+(-p+2v_y)\frac{\partial \phi^i_y|J|}{\partial h_j}+\phi^i_x\frac{\partial T_{xy}}{\partial h_j}+2\phi^i_y\frac{\partial T_{yy}}{\partial h_j}$$
$$+Re\,\phi^i u\Big(v_\xi\frac{\partial y_\eta}{\partial h_j}-v_\eta\frac{\partial y_\xi}{\partial h_j}\Big)+Re\,\phi^i v\Big(-v_\xi\frac{\partial x_\eta}{\partial h_j}+v_\eta\frac{\partial x_\xi}{\partial h_j}\Big)-N^2\Big(v_x\frac{\partial x}{\partial h_j}+v_y\frac{\partial y}{\partial h_j}\Big)\phi^i|J|\Big]\,\mathrm{d}\xi\,\mathrm{d}\eta, \tag{A 25}$$

$$\frac{\partial R^i_{mz}}{\partial h'_j} = N\iint\Big[-p\frac{\partial|J|}{\partial h_j}\phi^i/|J|-p\Big(\phi^i_x\frac{\partial x}{\partial h_j}+\phi^i_y\frac{\partial y}{\partial h_j}\Big)$$
$$+\phi^i_x\Big(u_x\frac{\partial x}{\partial h_j}+u_y\frac{\partial y}{\partial h_j}\Big)+\phi^i_y\Big(v_x\frac{\partial x}{\partial h_j}+v_y\frac{\partial y}{\partial h_j}\Big)\Big]|J|\,\mathrm{d}\xi\,\mathrm{d}\eta, \tag{A 26}$$

where
$$\frac{\partial T_{xx}}{\partial h_j}=\Big(u_\xi\frac{\partial \xi_x}{\partial h_j}+u_\eta\frac{\partial \eta_x}{\partial h_j}\Big)|J|,\quad \frac{\partial T_{yy}}{\partial h_j}=\Big(v_\xi\frac{\partial \xi_y}{\partial h_j}+v_\eta\frac{\partial \eta_y}{\partial h_j}\Big)|J|,$$
$$\frac{\partial T_{xy}}{\partial h_j}=\Big(u_\xi\frac{\partial \xi_y}{\partial h_j}+u_\eta\frac{\partial \eta_y}{\partial h_j}+v_\xi\frac{\partial \xi_x}{\partial h_j}+v_\eta\frac{\partial \eta_x}{\partial h_j}\Big)|J|.$$

Momentum boundary integral over free surface

$$\frac{\partial R^i_{mx}}{\partial h'_j}=\frac{1}{Ca}\int\Big[\frac{1}{g^{\frac12}}\frac{\partial x_\xi}{\partial h_j}\phi^i_\xi-\frac{x_\xi}{g^{\frac32}}\Big(x_\xi\frac{\partial x_\xi}{\partial h_j}+y_\xi\frac{\partial y_\xi}{\partial h_j}\Big)\phi^i_\xi-N^2\frac{y_\xi}{g^{\frac12}}\Big(x_\xi\frac{\partial y_z}{\partial h_j}-y_\xi\frac{\partial x_z}{\partial h_j}\Big)\phi^i\Big]\,\mathrm{d}\xi, \tag{A 27}$$

$$\frac{\partial R^i_{my}}{\partial h'_j}=\frac{1}{Ca}\int\Big[\frac{1}{g^{\frac12}}\frac{\partial y_\xi}{\partial h_j}\phi^i_\xi-\frac{y_\xi}{g^{\frac32}}\Big(x_\xi\frac{\partial x_\xi}{\partial h_j}+y_\xi\frac{\partial y_\xi}{\partial h_j}\Big)\phi^i_\xi+N^2\frac{x_\xi}{g^{\frac12}}\Big(x_\xi\frac{\partial y_z}{\partial h_j}-y_\xi\frac{\partial x_z}{\partial h_j}\Big)\phi^i\Big]\,\mathrm{d}\xi, \tag{A 28}$$

$$\frac{\partial R^i_{mz}}{\partial h'_j}=\frac{N}{Ca}\int\frac{1}{g^{\frac12}}\Big[\Big(x_\xi\frac{\partial x_\xi}{\partial h_j}+y_\xi\frac{\partial y_\xi}{\partial h_j}\Big)\phi^i+\Big(x_\xi\frac{\partial x_z}{\partial h_j}+y_\xi\frac{\partial y_z}{\partial h_j}\Big)\phi^i_\xi\Big]\,\mathrm{d}\xi, \tag{A 29}$$

where g is defined by
$$g=x_\xi^2+y_\xi^2.$$

These free-surface derivatives are computed by the chain rule and the isoparametric mapping, for example:
$$x_\xi=\sum x_i\phi^i_\xi,\quad |J|=x_\xi y_\eta-x_\eta y_\xi,$$
$$\frac{\partial \phi^i_x|J|}{\partial h_j}=\phi^i_\xi\frac{\partial y_\eta}{\partial h_j}-\phi^i_\eta\frac{\partial y_\xi}{\partial h_j},\quad \frac{\partial \phi^i_y|J|}{\partial h_j}=-\phi^i_\xi\frac{\partial x_\eta}{\partial h_j}+\phi^i_\eta\frac{\partial x_\xi}{\partial h_j}.$$

REFERENCES

BENJAMIN, T. B. 1978 Bifurcation phenomena in steady viscous flows of a viscous fluid. I. Theory; II. Experiments. *Proc. R. Soc. Lond.* A **359**, 1.

BENJAMIN, T. B. & MULLIN, T. 1981 Notes on the multiplicity of flows in the Taylor experiment. *J. Fluid Mech.* **121**, 219.

BENKREIRA, H., EDWARDS, M. F. & WILKINSON, W. L. 1982 Ribbing instability in the roll coating of Newtonian fluids. *Plastics Rubber Proc. Appl.* **2**, 137.

BIXLER, N. E. 1982 Stability of a coating flow. Ph.D. thesis, University of Minnesota, Minneapolis.

COLES, D. 1965 Transition in circular Couette flow. *J. Fluid Mech.* **21**, 385.

COYLE, D. J. 1984 The fluid mechanics of roll coating: steady flows, stability, and rheology. Ph.D. thesis, University of Minnesota, Minneapolis.

COYLE, D. J., MACOSKO, C. W. & SCRIVEN, L. E. 1986 Film-splitting flows in forward roll coating. *J. Fluid Mech.* **171**, 183.

COYNE, J. C. & ELROD, H. G. 1970 Conditions for the rupture of a lubricating film. Part I: Theoretical model; Part II: New boundary conditions for Reynolds equations. *Trans. ASME* F: *J. Lubric. Technol.* **92**, 451.

GOKHALE, V. V. 1983*a* Improved stability criterion for lubrication flow between counterrotating rollers. *AIChE J.* **29**, 865.

GOKHALE, V. V. 1983*b* Exact solution to the ribbing instability problem in lubrication flow by invariant imbedding. *Chem. Engng Commun.* **21**, 81.

GREENER, J. 1979 Bounded coating flows of viscous and viscoelastic fluids. Ph.D. thesis, University of Massachusetts.

GREENER, J., SULLIVAN, T., TURNER, B. & MIDDLEMAN, S. 1980 Ribbing instability of a two-roll coater: Newtonian fluids. *Chem. Engng Commun.* **5**, 73.

HOOD, P. 1976 Frontal solution program for unsymmetric matrices. *Intl J. Num. Meth. Engng* **10**, 379. Correction. *Intl J. Num. Meth. Engng* **11**, (1977) 1055.

IOOSS, G. & JOSEPH, D. D. 1980 *Elementary Stability and Bifurcation Theory*. Springer.

KEENER, J. P. & KELLER, H. B. 1973 Perturbed bifurcation theory. *Arch. Rat. Mech. Anal.* **50**, 159.

KISTLER, S. F. & SCRIVEN, L. E. 1983 Coating flows. In *Computational Analysis of Polymer Processing* (ed. J. R. A. Pearson & S. M. Richardson), p. 243. Applied Science Publishers.

KOGELMAN, S. & DIPRIMA, R. C. 1970 Stability of spatially periodic supercritical flows in hydrodynamics. *Phys. Fluids* **13**, 1.

MILL, C. C. & SOUTH, G. R. 1967 Formation of ribs on rotating rollers. *J. Fluid Mech.* **28**, 523.

PEARSON, J. R. A. 1960 The instability of uniform viscous flow under rollers and spreaders. *J. Fluid Mech.* **7**, 481.

PITTS, E. & GREILLER, J. 1961 The flow of thin liquid films between rollers. *J. Fluid Mech.* **11**, 33.

RUSCHAK, K. J. 1982 Boundary conditions at a liquid/air interface in lubrication flows. *J. Fluid Mech.* **119**, 107.

RUSCHAK, K. J. 1983 A three-dimensional linear stability analysis for two-dimensional free boundary flows by the finite element method. *Computer Fluids* **11**, 391.

RUSCHAK, K. J. 1985 Coating flows. *Ann. Rev. Fluid Mech.* **17**, 65.

SAFFMAN, P. G. & TAYLOR, G. I. 1958 The penetration of a fluid into a porous medium or Hele-Shaw cell containing a more viscous liquid. *Proc. R. Soc. Lond.* A **245**, 312.

SAVAGE, M. D. 1977*a* Cavitation in lubrication. Part 1. On boundary conditions and cavity-fluid interfaces. *J. Fluid Mech.* **80**, 743.

SAVAGE, M. D. 1977*b* Cavitation in lubrication. Part 2. Analysis of wavy interfaces. *J. Fluid Mech.* **80**, 757.

SAVAGE, M. D. 1984 Mathematical model for the onset of ribbing. *AIChE J.* **30**, 999.

STEWART, F. M. 1978 Simultaneous iteration for computing invariant subspaces of non-Hermitian matrices. *Numer. Maths* **25**, 123.

TAYLOR, G. I. 1923 Stability of a viscous liquid contained between two rotating cylinders. *Phil. Trans. R. Soc. Lond.* A **223**, 289.

TAYLOR, G. I. 1963 Cavitation of viscous fluid in narrow passages. *J. Fluid Mech.* **16**, 595.

WEATHERBURN, C. E. 1929 *Differential Geometry of Three Dimensions*. Cambridge University Press.